

1 Investigating the Role of Gravity Waves on Mesosphere-Lower-Thermosphere

2 (MLT) Inversion Layers at Low Latitudes (3-15°)

3 Chalachew Lingerew^{1*}, U. Jaya Prakash Raju¹

4 ¹ Department of Physics, Washera Geospace, and Radar Science Laboratory, Bahir Dar
5 University, Bahir Dar, Ethiopia

6 *Correspondence to:* Chalachew Lingerew (chalachewlingerew@gmail.com)

7 **Abstract**

8 The Mesosphere and Lower Thermosphere (MLT) transitional region, encompassing a height
9 range of 60-100 km, is a distinct and highly turbulent zone within the Earth's atmosphere. This
10 region is particularly significant due to dynamic processes like gravity waves, which contribute
11 to the formation of the Mesospheric Inversion Layer (MIL). Investigating these phenomena is
12 crucial for understanding the dynamics of the middle and upper atmosphere, especially regarding
13 stability and energy transfer. Inversion layers significantly influence the stability of the
14 atmosphere in this region, playing a crucial role in atmospheric dynamics. Inversion layers are
15 associated with energy transfer processes, vital for understanding the overall dynamics of the
16 atmosphere. Despite extensive study on an inversion, the formation mechanisms of mesospheric
17 inversions remain poorly understood. This article explores the upper and lower inversion
18 phenomena and their causative mechanisms. It uses long-term SABER observations from 2005
19 to 2020 over the latitude range of 3-15° N and longitude range of 33-48° E. The results show that
20 the upper inversion occurs more frequently, with a frequency below 40%, compared to the lower
21 inversion, which occurs below 20%. The upper inversion occurs within the height range of 78-
22 91 km, with an inversion amplitude of approximately 20-80 K and a thickness of around 3-12
23 km. In contrast, the lower inversion is confined to the height range of 70-80 km, with an
24 inversion amplitude of about 10-60 K and a thickness of around 4-10 km. Moreover, the gravity
25 wave indicator potential energy shows high energy (below 100 J/kg) in the upper mesosphere
26 region (85-90 km) compared to the lower mesosphere region (70-75 km) with less than 50 J/kg.
27 Considering gravity waves, the Brunt-Väisälä frequency (N^2) stability criteria indicate instability
28 in the upper mesosphere region with very low values compared to the lower mesosphere region.
29 This suggests that the high amount of gravity wave potential energy is a consequence of the
30 higher instability in the upper inversion compared to the lower inversion.

31 **Keywords:** Mesosphere and Lower Thermosphere (MLT), Upper and Lower Inversions,
32 Perturbed Temperature, Causative Gravity Waves, Potential Energy, Brunt-Väisälä Frequency,
33 Atmospheric Instability.

34 **Introduction**

35 The Mesosphere and Lower Thermosphere (MLT) region serves as a transitional zone for wave
36 processes from the lower and upper atmospheres, including tidal, planetary, and gravity waves.
37 Gravity waves (GWs) originating from the lower atmosphere are known to propagate into the
38 mesosphere. There, they break and dissipate their energy and momentum, affecting the thermal
39 structure, global atmospheric circulation, and variability of the mesosphere. This process also
40 influences the formation of mesospheric inversion layers (MILs), which are associated with
41 increased temperature variability in the mesosphere. MILs indicate wave saturation when the
42 lapse rate falls below the dry adiabatic lapse rate (Sica et al., 2007). Temperature inversions in
43 the mesosphere have been widely observed and studied using various techniques, including lidar,
44 radar, rocket sondes, and satellites, across different geographic locations. Sivakandan et al.
45 (2014) utilized TIMED/SABER kinetic temperature data to examine the occurrence and
46 characteristics of mesospheric inversions over the equatorial Indian region (0 to 10° N and 70 to
47 90° E) for the years 2002 and 2008. However, they did not explore the causative factors. This
48 study aims to investigate the causes of these inversions, focusing specifically on the role of
49 atmospheric gravity waves.

50 Gravity waves and mesospheric inversion layers (MILs) are interconnected phenomena within
51 the Earth's atmosphere, particularly in the mesosphere and lower thermosphere. MILs are layers
52 within the mesosphere where the temperature profile shows an inversion. This means the
53 temperature increases with altitude, contrary to the typical decrease. These inversion layers often
54 form due to dynamic processes, including the breaking and dissipation of gravity waves. As
55 gravity waves propagate upwards, they can grow in amplitude because the atmospheric density
56 decreases with altitude. When these waves reach a critical amplitude, they become unstable and
57 break. This breaking process releases energy and momentum into the surrounding air, causing
58 localized heating. The energy dissipation from breaking gravity waves causes localized heating.
59 This heating can create or enhance mesospheric inversion layers by increasing the temperature at
60 certain altitudes. The breaking of gravity waves can also generate turbulence, which further
61 influences the structure and stability of inversion layers. This process also contributes to
62 momentum and energy deposition.

63 The momentum and energy deposition of gravity waves (GWs) are believed to be key drivers of
64 large-scale atmospheric circulation, the coupling of different atmospheric layers, and inversion
65 phenomena (Fritts and Alexander, 2003; Lindzen, 1981; Smith, 2012). Additionally, researchers

66 are exploring the influence of gravity wave-breaking on mesosphere dynamics to understand its
67 impact on inversion phenomena, particularly in mid- and high-latitude regions (Gan et al., 2012;
68 Walterscheid and Hickey, 2009; Collins et al., 2011; Szewczyk et al., 2013). Both observational
69 and modeling studies have investigated GWs as a cause of these inversions (Fritts, 2018; Collins
70 et al., 2014; Sridharan et al., 2008; Ramesh and Sridharan, 2012; Ramesh et al., 2013, 2014,
71 2017). Despite extensive exploration, our understanding of the impact of gravity waves on
72 mesosphere inversions, particularly in terms of temperature variability, remains incomplete,
73 especially in mid- and high-latitude regions (Singh and Pallamraju, 2018; Fritts et al., 2018). As
74 a result, the study of inversion phenomena and their underlying causes remains a key area of
75 focus in mesosphere dynamics research.

76 Research on the temporal and spatial variability of the mesosphere inversion phenomenon,
77 particularly about atmospheric waves and gravity wave activity, is notably lacking in low
78 latitudes. To address this gap, our study investigates the mesosphere inversion phenomenon and
79 its association with gravity wave activity and stability criteria. We use Brunt-Vaisala frequency
80 (N^2) over the low latitudinal band (3° – 15° N) with long-term SABER observations from 2005 to
81 2020. The study is organized as follows: Section 2 details the data and methodology used to
82 analyze the mesosphere inversion phenomenon and their causative gravity waves via the
83 potential energy. Section 3 presents the results, and Section 4 concludes the findings.

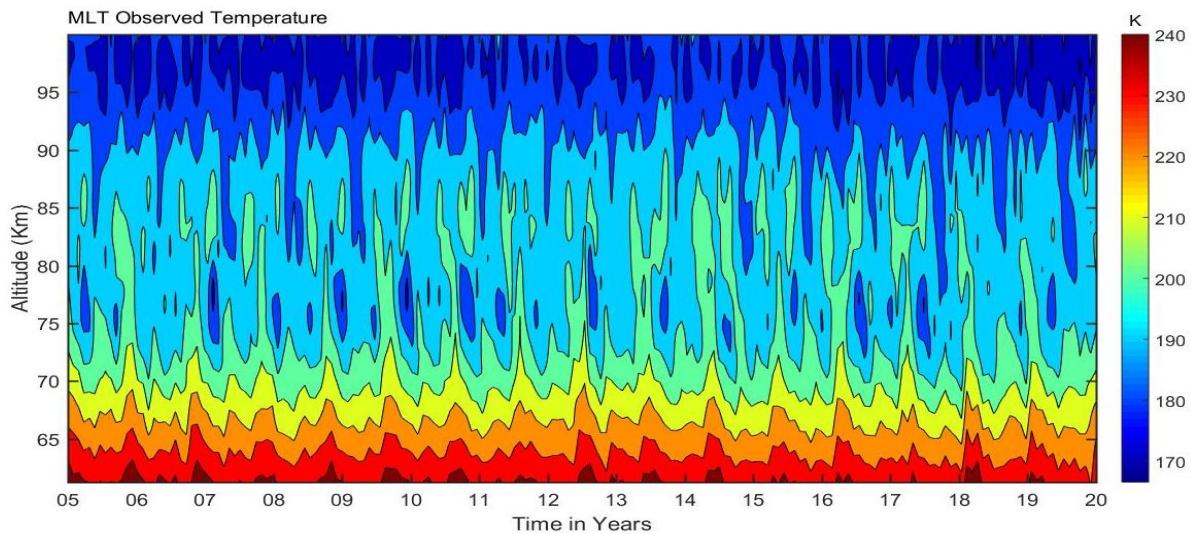
84 **2. Observation and Data analysis**

85 **2.1 SABER Observation**

86 The TIMED/SABER satellite, launched on December 7, 2001, operates in an elliptical orbit at
87 approximately 625 km altitude with a 74° inclination relative to the equator. Since its launch,
88 SABER has been a crucial tool for atmospheric research, providing extensive data on the middle
89 atmosphere. SABER is a limb-viewing radiometer working in the infrared region (1.27–17
90 microns) and can measure radiative emissions across a wide range of altitudes. It offers nearly
91 global coverage and continuous 24-hour data over 60 days. The instrument completes 15 orbits
92 daily, each taking about 97 minutes, and collects around 1400 data profiles per day, with each
93 profile taking 58 seconds. SABER's high-resolution temperature profiles are essential for
94 studying the dynamics and wave processes in the mesosphere. It provides temperature
95 measurements with an accuracy of 1 to 2 K between 15 and 60 km. The accuracy decreases to 5
96 K below 85 km and increases to 6.7 K to 10 K near 100 km. This data has been instrumental in
97 understanding the thermal structure and dynamical processes in the mesospheric region, as

98 highlighted by various studies (Garcia et al., 2008; Gan et al., 2012, 2014; Bizuneh et al., 2022;
99 Lingerew et al., 2023; Rezac et al., 2015; Meriwether and Gerrard, 2004; Fechine et al., 2008;
100 Dou et al., 2009; France et al., 2015).

101 We utilized SABER vertical temperature profiles taken within the 60–100 km altitude range.
102 These profiles cover the period from 2005 to 2020, spanning latitudes from 3°N to 15°N and
103 longitudes from 33°E to 48°E. Figure 1 shows the monthly mean of SABER temperature data for
104 the mesosphere and lower thermosphere. The data aim to illustrate the MLT temperature
105 variability, which helps us identify the inversion layers (MIL). The monthly mean temperatures
106 in the MLT region show a maximum of 200-240 K at altitudes of 60-70 km. Then it decreases to
107 around 160-180 K at 95-100 km throughout the entire period. While the temperature patterns in
108 the 70-90 km altitude range suggest an inversion, these inversions are not visible.



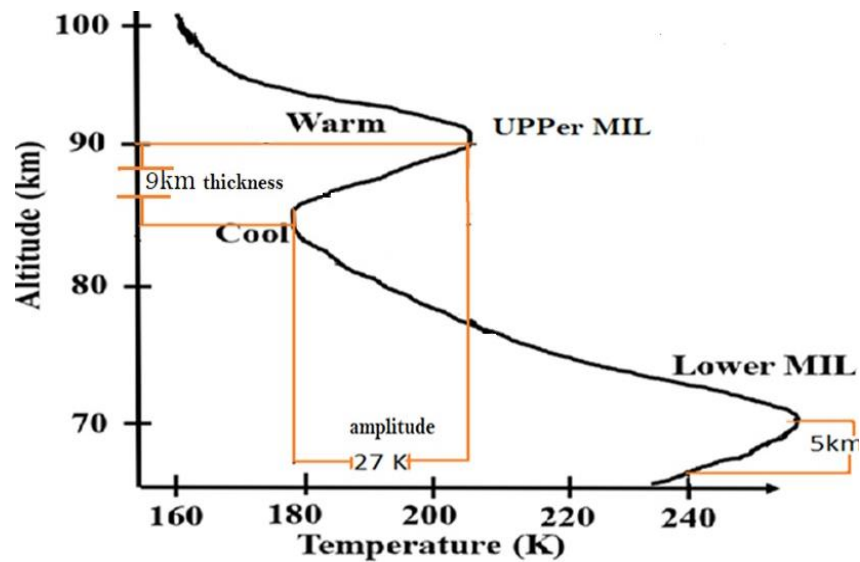
109
110 **Figure 1.** The monthly mean of MLT temperature variability in the height range of 60-100 km
111 during 2005-2020 over the low-latitude.

112 **2.2 Analysis Technique**

113 The Earth's middle atmosphere typically has a negative temperature gradient, but some reports
114 have shown positive temperature gradients in the mesosphere (Meriwether and Gardner, 2000;
115 Gan et al., 2012). This phenomenon is called the “mesospheric inversion layer (MIL)”. MILs are
116 identified using a procedure detailed by Leblanc and Hauchecorne (1997) and Fechine et
117 al.(2008). Mesospheric inversions are characterized by their thickness (the altitude difference
118 between maximum warming and cooling) and amplitude (the temperature difference between

119 these points) (Meriwether and Gardner, 2000). Here are the identification criteria for these
120 inversions:

- 121 1. The bottom level of the lower inversion is above 70 km, and the top level is below 80 km.
122 For the upper inversion, the bottom level is above 80 km, and the top level is below 92
123 km.
- 124 2. The amplitude is considered larger than 5 K.
- 125 3. The thickness is greater than or equal to 3 km.



126
127 Figure 2. Schematic of upper and lower mesospheric inversion layers shown in the temperature
128 profile for the MLT regions (Adapted from Meriwether and Gerrard, 2004).

129 Figure 2 illustrates this concept, showing a positive temperature difference between the top and
130 bottom levels of the inversion. This method has been utilized in numerous previous studies
131 investigating mesospheric inversions (Leblanc et al., 1998; Meriwether and Gardner, 2000; Duck
132 et al., 2001; Duck and Greene, 2004; Cutler et al., 2001; Siva Kumar et al., 2001; Ratnam et al.,
133 2003; Gan et al., 2012). The frequency occurrence rate of mesospheric inversion layers (MILs) is
134 derived during the period 2005–2020 in the upper and lower MLT regions. This rate is calculated
135 by dividing the number of inversion days in each month by the total number of days in that
136 month over the 16-year observation period (2005–2020).

137 Mesospheric temperature inversions are related to instabilities in atmospheric dynamics. To
138 identify the causative, short-period atmospheric gravity waves, a high-pass filter with a one-hour

139 interval cutoff frequency is applied using the Brunt-Väisälä frequency (N²). Another important
 140 concept to estimate the Brunt-Vaisala frequency is the potential temperature (θ). It represents the
 141 air parcel's temperature when it is displaced adiabatically to a standard pressure level, p_0 , from
 142 the current pressure level, p . This is based on the first law of thermodynamics.

$$143 \quad \frac{dT}{T} = \frac{R}{c_p} \frac{dp}{p} \Rightarrow \int_T^0 \frac{dT}{T} = \int_p^{p_0} \frac{R}{c_p} \frac{dp}{p} \quad (1) \text{ it yields}$$

$$144 \quad \theta = T \left(\frac{p_0}{p} \right)^{R/c_p} \quad (2)$$

145 Therefore, the motion of a vertical atmospheric air parcel can be described by (Liu, 2011; Vadas
 146 and Fritts, 2005) as follows in equation (2.3). This equation calculates the Brunt-Vaisala
 147 frequency of the parcel due to the buoyant and gravitational forces acting on it.

$$148 \quad \frac{d^2s}{dt^2} = -g \frac{\rho - \rho_0}{\rho} \sin a \quad (3)$$

149 Based on the hydrostatic equation, $\rho = \rho_0$, and $p = p_0 \Rightarrow \frac{\partial p}{\partial z} = \frac{\partial p_0}{\partial z} = -g\rho_0$ (4) and the ideal gas
 150 law, $\rho = p/RT = p_0/RT$ gives the parcels motion of an equation:

$$151 \quad \frac{d^2s}{dt^2} = -\frac{g}{\rho} \left(\frac{d\rho}{dp} \frac{\partial p_0}{\partial z} - \frac{\partial \rho_0}{\partial z} \right) z \quad (5)$$

152 Following the same approach using the hydrostatic equation (4) and adiabatic equation (6)

$$153 \quad d \ln \rho = \frac{d \ln p}{\gamma}, \gamma = c_p/c_v \quad (6) \text{ yields}$$

$$154 \quad \frac{d^2s}{dt^2} = -\frac{g}{\rho} \left(\frac{\rho}{\gamma p_0} \frac{\partial p_0}{\partial z} - \frac{\partial \rho_0}{\partial z} \right) z = g \left(\frac{\partial \ln \rho_0}{\partial z} - \frac{1}{\gamma} \frac{\partial \ln p_0}{\partial z} \right) z \quad (7)$$

156 For the ideal gas law of $p = \rho RT$, the natural logarithm is taken for altitude, z on both sides,
 157 yielding

$$158 \quad \frac{\partial \ln \rho}{\partial z} = \frac{\partial \ln p}{\partial z} - \frac{\partial \ln T}{\partial z} \quad (8)$$

159 Then after, the potential temperature (θ) of the parcel is calculated as follows based on the
 160 equation (2):

$$161 \quad \frac{\partial \ln \theta}{\partial z} = \frac{\partial \ln T}{\partial z} - \frac{R}{c_p} \frac{\partial \ln p}{\partial z} = \frac{1}{T} \left(\frac{\partial T}{\partial z} + \frac{g}{c_p} \right) = \left(1 - \frac{R}{c_p} \right) \frac{\partial \ln p}{\partial z} - \frac{\partial \ln \rho}{\partial z} \quad (9) \text{ to derive the}$$

162 Parcels acceleration based on equations (7) to become:

$$163 \quad \frac{d^2s}{dt^2} = -g \frac{\partial \ln \theta_0}{\partial z} z \sin a = -g \frac{\partial \ln \theta_0}{\partial z} ds \cdot \sin^2 a \quad (10)$$

164 Whereas by introducing the frequency, N, with $N^2 = g \frac{\partial \ln \theta_0}{\partial z}$

165 The Brunt-Vaisala frequency, N^2 is calculated based on the following mathematical formulation
 166 used to characterize atmospheric stability.

$$167 \quad N^2(z) = \frac{g(z)}{T_0(z)} \left(\frac{\partial T_0(z)}{\partial z} + \Gamma_d \right) \quad (11)$$

168 Where g is the acceleration due to gravity, N is the Vaisala frequency, T_0 is the background
 169 temperature (estimated based on third-order polynomial fitting), $\Gamma_d = g/c_p$ is the adiabatic lapse
 170 rate, and $c_p = 1004 J K^{-1} kg^{-1}$ is the specific heat capacity of the atmosphere at constant
 171 pressure. When the Vaisala frequency, N^2 , is positive, the atmosphere is stable. When N^2 is
 172 negative, the atmosphere is unstable. In this case, the atmospheric lapse rate, $\Gamma = -\frac{\partial T}{\partial z}$, is larger
 173 than the adiabatic lapse rate, $g/c_p \approx 9.5 K km^{-1}$. To estimate the Brunt-Vaisala frequency, a
 174 third-order polynomial fit of the least squares has been applied to the SABER observed
 175 temperature (T) profile to estimate the background temperature (T_0), following the procedure of
 176 Leblanc and Hauchecorne (1997). After estimating the perturbed temperature (T_p) from equation
 177 (12), it is identified by subtracting the background temperature from the observed temperature
 178 data (T).

$$179 \quad T_p = T - T_0 \quad (12)$$

180 After estimating the perturbed temperature (T_p), a high-pass band filter is applied. This filter
 181 removes low-frequency components associated with planetary and tidal waves, retaining the
 182 high-frequency components related to short-period gravity waves (John and Kumar, 2012). This
 183 process isolates the influence of gravity waves and accurately calculates their potential energy.

184 **The high-pass filter is based on known frequency ranges, typically below the period one-hour).**

$$185 \quad E_p(z) = \frac{1}{2} \left(\frac{g(z)}{N(z)} \right)^2 \left(\frac{T_p'(z)}{T_0(z)} \right)^2 \quad (13)$$

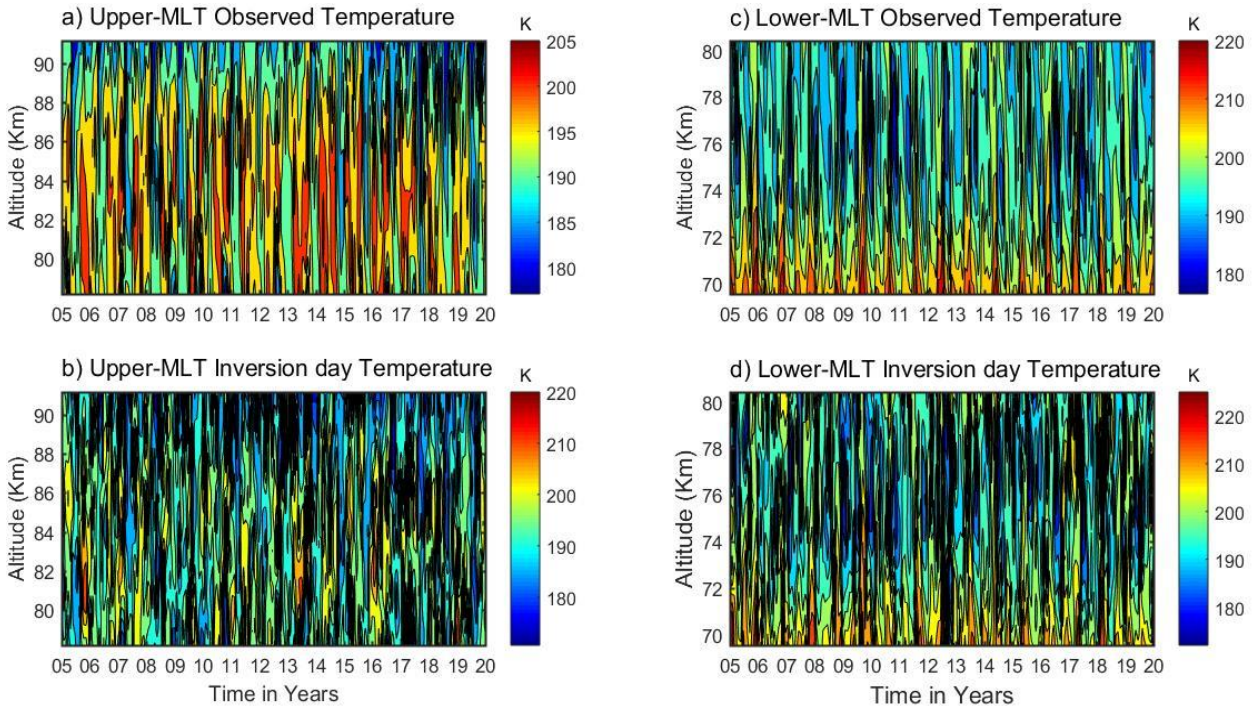
186 The potential energy of the waves, a function of altitude (z), is used to determine the impact of
 187 atmospheric gravity waves on atmospheric inversions.

188 **3. Results and discussion**

189 **3.1 Identification and Characteristics of the Lower and Upper MLT Inversion**

190 Daily SABER temperature profiles, covering altitudes of 60–100 km from 2005 to 2020, are
 191 shown in the contour plots of Figure 3. Figures 3 (a and b) depict the upper mesosphere, while
 192 Figures 3 (c and d) show the lower mesosphere. The horizontal panels of Figures 3 (a) and 3 (c)
 193 show observed temperatures ranging from approximately 180–220 K, before accounting for

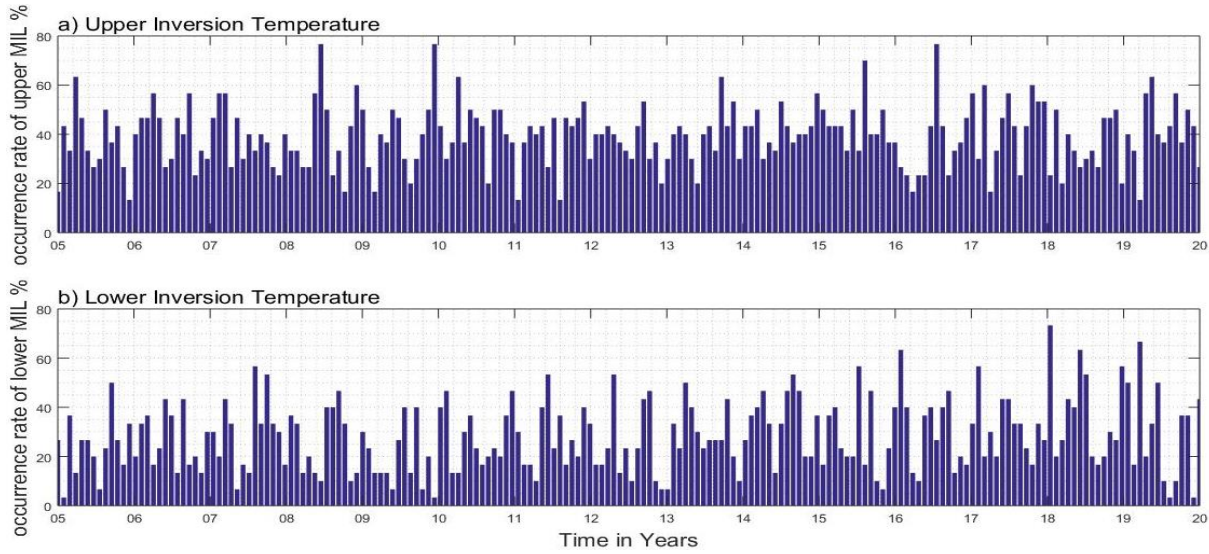
194 inversion layers. The horizontal panels of Figures 3 (b) and 3 (d) show inversion day
 195 temperatures, ranging from 180–225 K. These inversion day temperatures are higher than those
 196 shown in Figures 3 (a) and 3 (c). This indicates that maximum temperatures occur on inversion
 197 days in both the upper and lower MLT regions.



198 **Figure 3.** The upper and lower mesosphere observed temperatures in the first horizontal panel at
 199 (a and c) with their inversions in the second horizontal panel at (b and d).
 200

201 The upper left panel of Figure 3(a) shows the observed temperature in the upper mesosphere. It
 202 ranges from approximately 180–205 K at altitudes of around 80–90 km. The upper right panel of
 203 Figure 3(c) shows the lower mesosphere, with temperatures ranging from about 180–220 K at
 204 altitudes of approximately 70–80 km. In contrast, the lower left panel of Figure 3(b) shows an
 205 upper-mesosphere inversion day temperature. It ranges from 180–220 K at an altitude of
 206 approximately 80–90 km. The lower right panel of Figure 3(d) shows a lower-mesosphere
 207 inversion day temperature. It ranges from 180–225 K at an altitude of approximately 70–80 km.
 208 These inversion day temperatures in Figures 3(b) and 3(d) suggest a temperature gradient
 209 shifting from negative to positive. This could be due to factors such as atmospheric gravity
 210 waves, chemical reactions, or solar radiation. Our temperature observations for the lower MLT
 211 region on an inversion day, within the altitudinal range of 70–80 km, align with those reported
 212 by Sivakumar et al. (2001). They identified inversion day temperature variability in the
 213 altitudinal range of 73–79 km. Additionally, Sivakandan et al. (2014) examined mesospheric

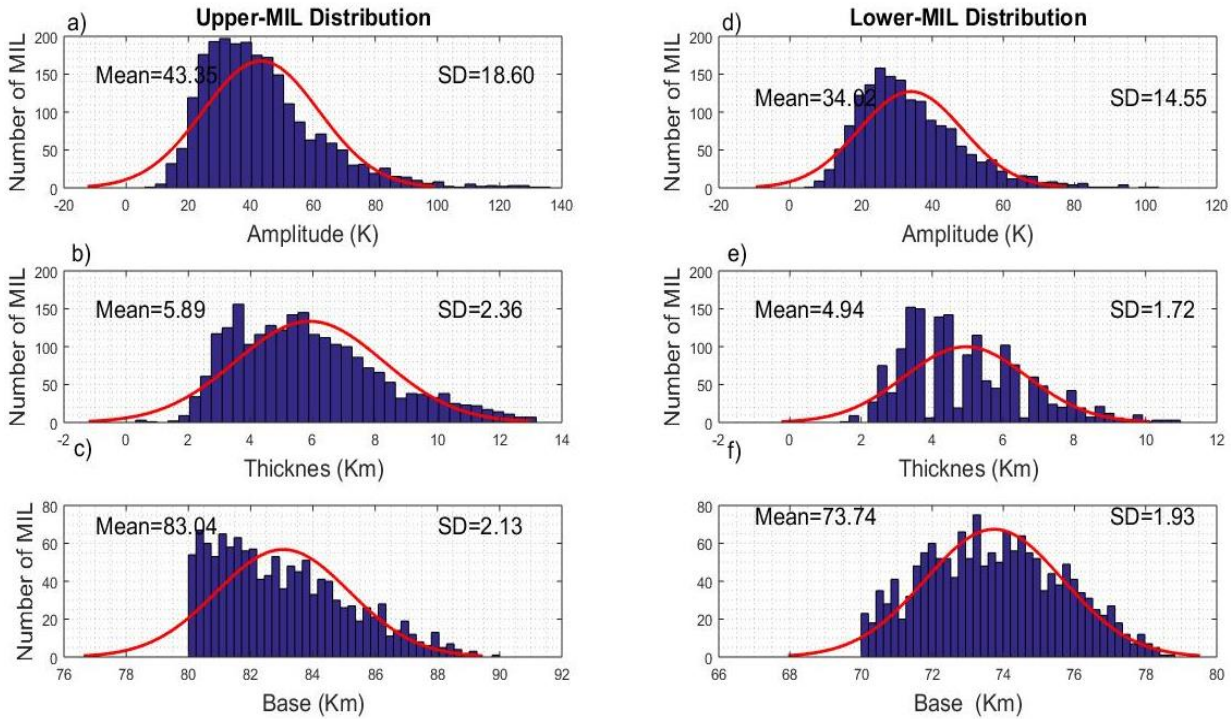
214 inversions in the 60–105 km altitude range over low-latitude regions. Their findings closely
215 match our results.



216
217 **Figure 4.** The frequency occurrence rate (percentage) of the (a) upper and (b) lower inversion
218 temperatures during 2005-2020 over low latitudes.

219 Figure 4 shows the frequency occurrence rate (%) of mesospheric inversion layers (MILs) in
220 histograms. Figure 4(a) shows the occurrence rate for upper MILs, while Figure 4(b) shows the
221 rate for lower MILs. The mean frequency occurrence rate of upper inversions is approximately
222 below 40%. Peak rates range from 60% to 78%, notably in the years 2008, 2010, and mid-2016.
223 In contrast, the mean occurrence rate for lower inversions is below 20%. Overall, the occurrence
224 rate for upper inversions is relatively higher compared to lower inversions. This may be related
225 to atmospheric wave activities, mainly gravity waves. Hauchecorne et al. (1987) and France et al.
226 (2015) discuss the effects of gravity waves on inversion variability in the upper and lower
227 mesosphere. Based on these findings, Figure 5 examines the characteristics of inversion layers,
228 including their amplitude and thickness. Figure 5 illustrates the characteristics of mesospheric
229 temperature variability on an inversion day. It focuses on base height, amplitude, and thickness,
230 before examining the effects of gravity waves on an inversion. Histograms show the frequency
231 of amplitude, thickness, and base height for inversion day MLT temperature variability. These
232 histograms feature best-fit Gaussian distribution curves, represented by red lines. The observed
233 distributions align with Gaussian curves, indicating that the number of mesospheric inversion
234 layers (MILs) follows a normal distribution. This suggests that the attributes are real-valued
235 random variables. The left column has three rows showing histograms of (a) amplitude, (b)
236 thickness, and (c) base height of the inversion day temperature variability for the upper MLT.

237 These histograms also include their statistical values, mean, and standard deviations (SD). The
 238 corresponding right column has three rows representing (d) amplitude, (e) thickness, and (f) base
 239 height of the inversion day temperature variability for the lower MLT region.



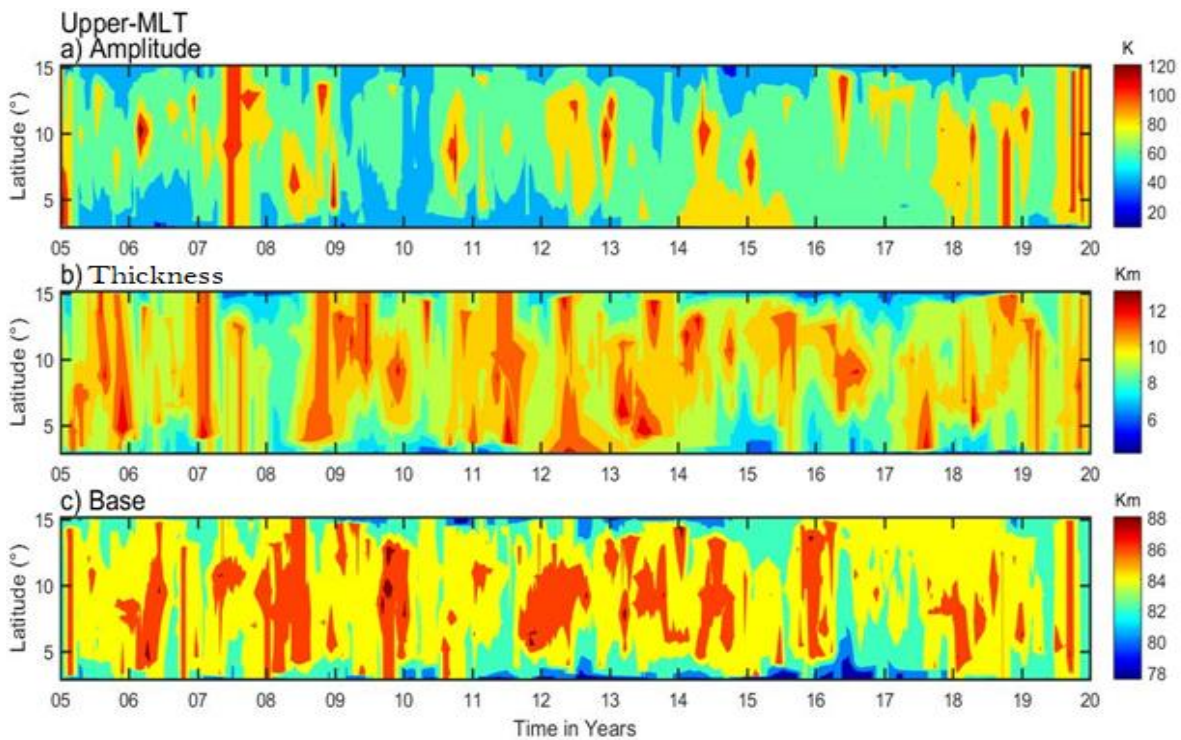
240
 241 **Figure 5.** The histograms depict the occurrence of MLT inversion day temperature variability.
 242 The first vertical panel shows the distribution of (a) amplitude, (b) thickness, and (c) base height
 243 for the upper inversion day. The second vertical panel presents the corresponding distribution for
 244 the lower inversion, including (d) amplitude, (e) thickness, and (f) base height.

245 The amplitude of upper inversion day temperature variability in Figure 5(a) ranges between 20
 246 and 80 K, with a peak value of 38 K. This follows a Gaussian distribution with a large standard
 247 deviation (SD) of 18.6. The thickness of the inversion layer for upper MILs, shown in Figure
 248 5(b), ranges from 3 to 9 K. The most probable value is 5.5 K, with a low SD of 2.3. The base
 249 height of the upper MIL in Figure 5(c) spans from ~80 to 90 km, with a peak value of around 83
 250 km. This indicates a large number of upper MLT inversions, with an SD of 2.13. The highest
 251 number of upper inversions between 2005 and 2020 is observed at 82 km. This may be attributed
 252 to gravity wave breaking and energy dissipation, influenced by waves generated from lower
 253 atmospheric regions and solar flux impacts. The lower inversion amplitude, depicted in Figure
 254 5(d), ranges between 10 and 60 K, with a peak value of 25 K and a standard deviation (SD) of
 255 14.5. The thickness of the lower inversion, shown in Figure 5(e), ranges from 3 to 8 km, with the
 256 most probable value at 3.8 km and a low SD of 1.72. The base height of the lower inversion in

257 Figure 5(f) ranges from 70 to 80 km, with a peak value of around 74 km and a lower SD of 1.93.
 258 Previous investigations by Sivakandan et al. (2014) from the Indian sector reported amplitudes
 259 ranging from 14–39 K in 2002 and 15–42 K in 2008. The thicknesses ranged between 2.7–7.5
 260 km in 2002 and 2.8–7.3 km in 2008, under the influence of solar flux. These findings align well
 261 with the present study, indicating no significant variation in characterizing mesospheric inversion
 262 based on amplitude and thickness in the low-latitude region within the altitude range of 60 to 90
 263 km.

264 **3.2 Latitudinal Variations of Mesospheric Inversion Layers (MILs)**

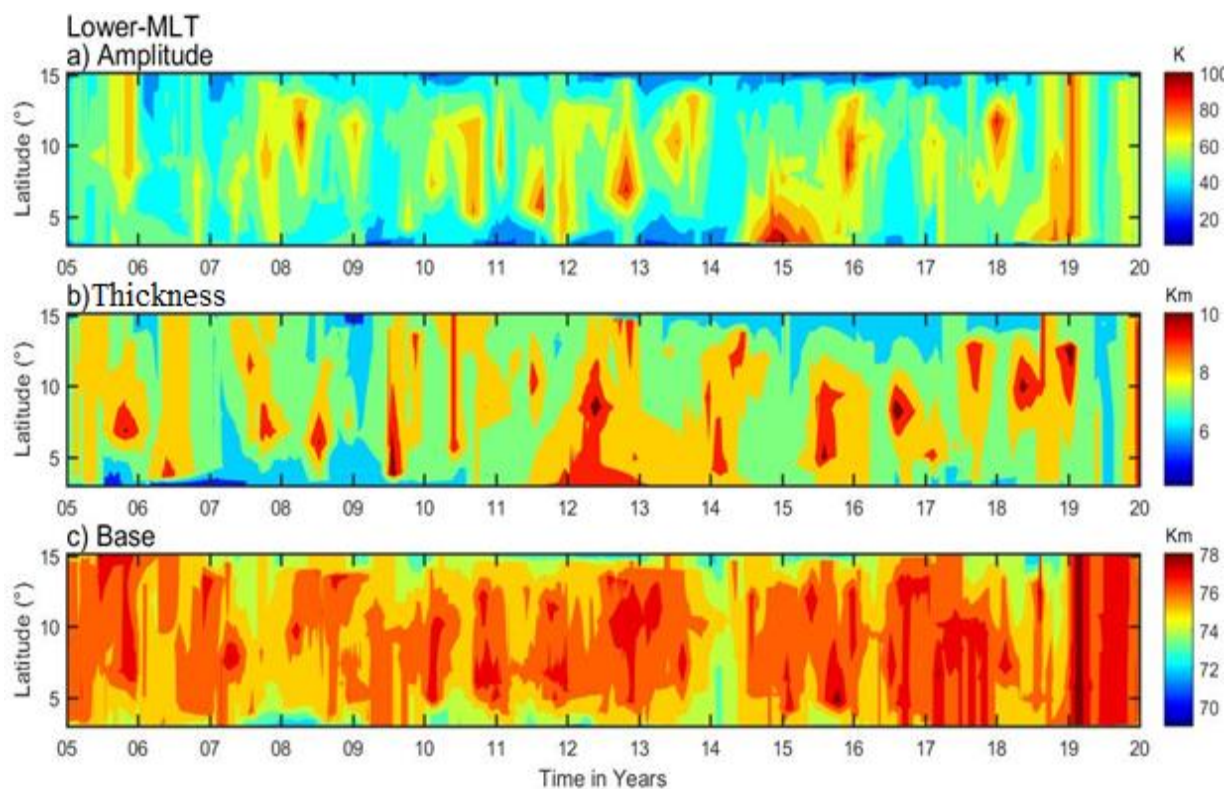
265 This section examines the spatiotemporal (latitudinal-time) variability of upper and lower
 266 mesosphere inversion phenomena. Contour plots of time vs. latitude in Figures 6 and 7,
 267 respectively, characterize this variability based on amplitude, thickness, and base height over the
 268 low-latitude band (3-15°) during 2005–2020. The Upper MILs phenomenon is observed around
 269 80–90 km. The maximum amplitude, in the range of 90–120 K, occurs over latitude bands (5-
 270 12°) during 2005, 2007, mid-2011, 2013, 2015, 2016, mid-2019, and 2020 (Figure 6(a)). The
 271 second horizontal panel in Figure 6(b) shows the inversion thickness, with a maximum range of
 272 ~ (8–12 km) across the entire latitudinal region (3-15° N). Figure 6(c) shows the relative
 273 maximum inversion base height, around ~ (84-88 km), in the latitudinal range between 4° and 14°
 274 N during 2006, 2008, 2010, 2012, 2016, and 2018.



275

276 **Figure 6.** The daily upper inversions (~80-90 km) of (a) amplitude, (b) thickness, and (c) base
277 height during 2005-2020 over latitudinal variation.

278 Contour plots in Figure 7(a, b, and c) show the latitudinal variations of the lower inversion
279 (MILs) phenomenon, based on amplitude, thickness, and base height, respectively. These plots
280 cover an altitudinal range of ~70-80 km. The lower inversion amplitude generally ranges from
281 ~30-60 k across all latitudinal bands. However, it reaches a maximum range of ~(80-100 k)
282 during 2013, 2015, 2016, and 2019 in various latitudinal regions between 5 and 140 N. Figure
283 7(b) shows an inversion thickness of 5-7 km across the entire latitude band, except for a
284 maximum thickness of 8-10 km. Figure 7(c) shows a base height of 76-80 km for most latitudes
285 and periods. However, there are exceptions: 2008, 2014, and mid-year 2018 exhibit a maximum
286 base height.



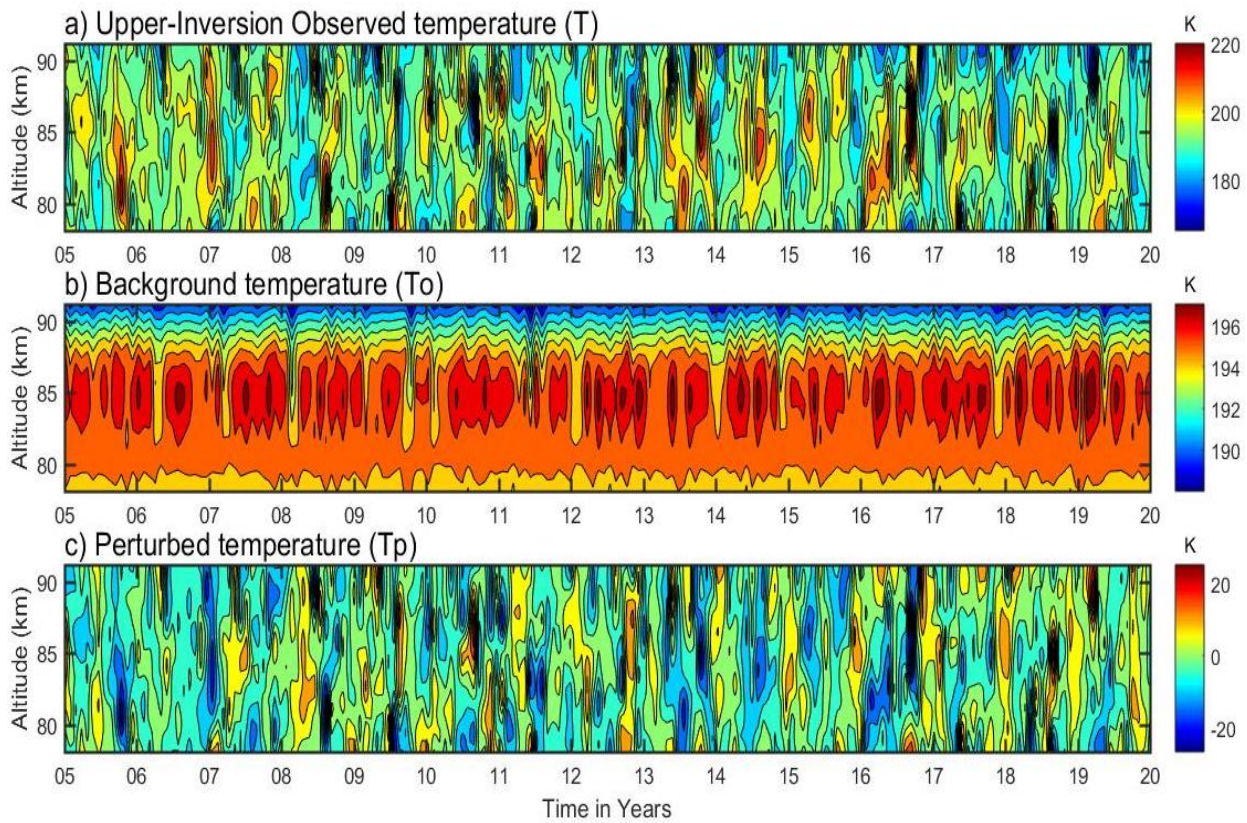
287 **Figure 7.** Same as Figure 5, but for the lower mesosphere inversions (~70- 80 km).
288

289 Figures 6 and 7 demonstrate that the upper inversion exhibits higher amplitude and thickness
290 compared to the lower inversion, suggesting a highly dynamic phenomenon in the upper
291 mesosphere region. Satellite measurements, particularly those from TIMED/SABER, provide
292 valuable insights into latitudinal variations in MILs. These observations confirm that MILs also
293 occur at low latitudes (Gan et al., 2012).

294

3.3 Separations of the Perturbed Temperature in the Mesosphere Region

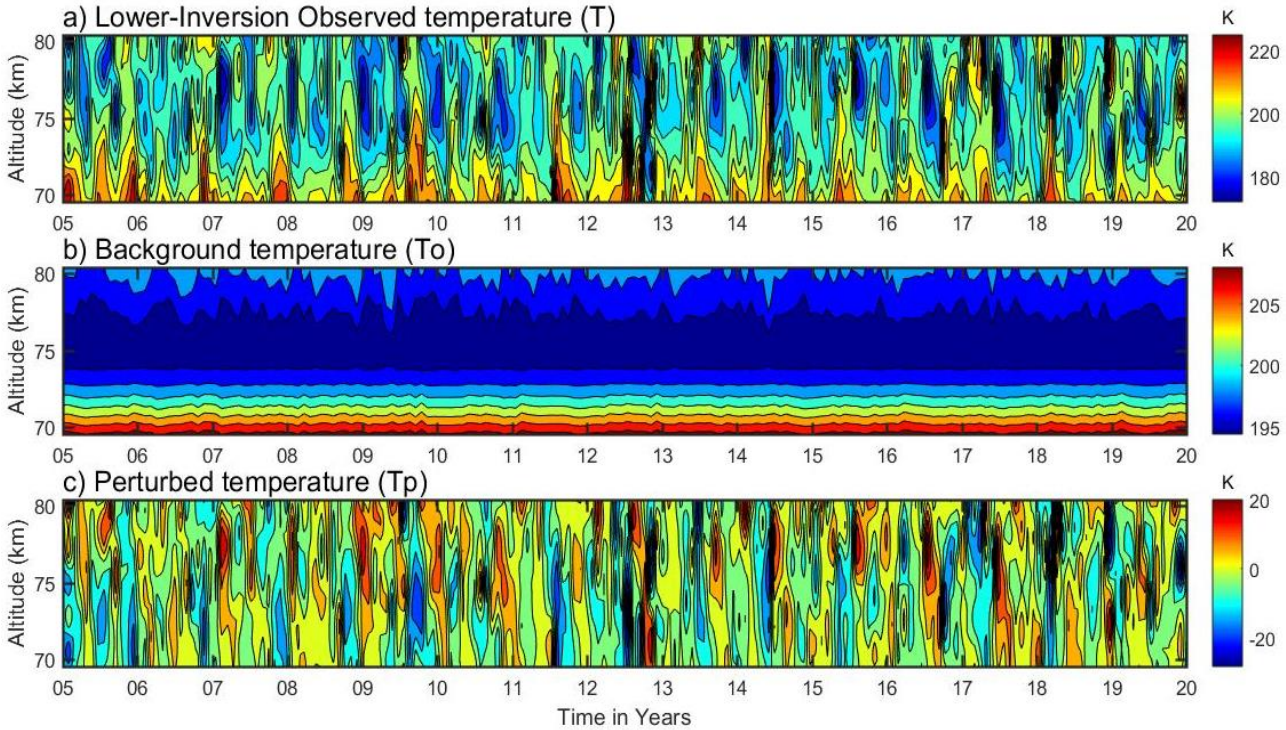
The perturbed temperature (T_p) of the upper and lower MLT inversions during the period of 2005-2020 can further be used to calculate their derived potential energy of gravity waves and the Brunt-Väisälä frequencies (N^2). First, the upper-temperature inversion profiles are identified in the MLT region during the entire observational period of 2005-2020, as displayed in the contour plot of Figure 8(a). The observed temperature ranges from ~170-220 K with minimal variability. A 3rd-order polynomial fit is applied to calculate the background temperature (T_0), as shown in the contour plot of Figure 8(b). This background temperature exhibits periodic variability over an altitude of around ~82-87 km, ranging from ~195-197 K. The perturbed temperature profiles (T_p), calculated as the difference between the observed inversion temperature (T) and the corresponding background temperature profiles (T_0), range from -25 to +25 K, as shown in Figure 8(c).



307 **Figure 8.** The upper mesosphere temperatures in the vertical panel are: (a) inversion day
308 observed temperature; (b) background temperature; and (c) perturbed temperature in the upper
309 mesosphere region.
310

311 A similar procedure is used to calculate the perturbed temperature (T_p), observed temperature,
312 and background temperature in the lower mesosphere region from 2005 to 2020. Their

313 corresponding contours are displayed in Figure 9(a-c). In Figure 9(a), the observed temperature
 314 of the lower inversion ranges from ~170-220 K. The background temperature of the lower
 315 inversion ranges from ~ 195-210 K, with maximum values of ~200-210 K at a height of ~70-72
 316 Km, as shown in Figure 9(b). The perturbed temperature in Figure 9(c) ranges from -25 to 20 K.
 317 Notably, the upper mesosphere perturbed temperature is at its maximum compared to the lower
 318 mesosphere region, possibly due to a highly dynamic phenomenon.

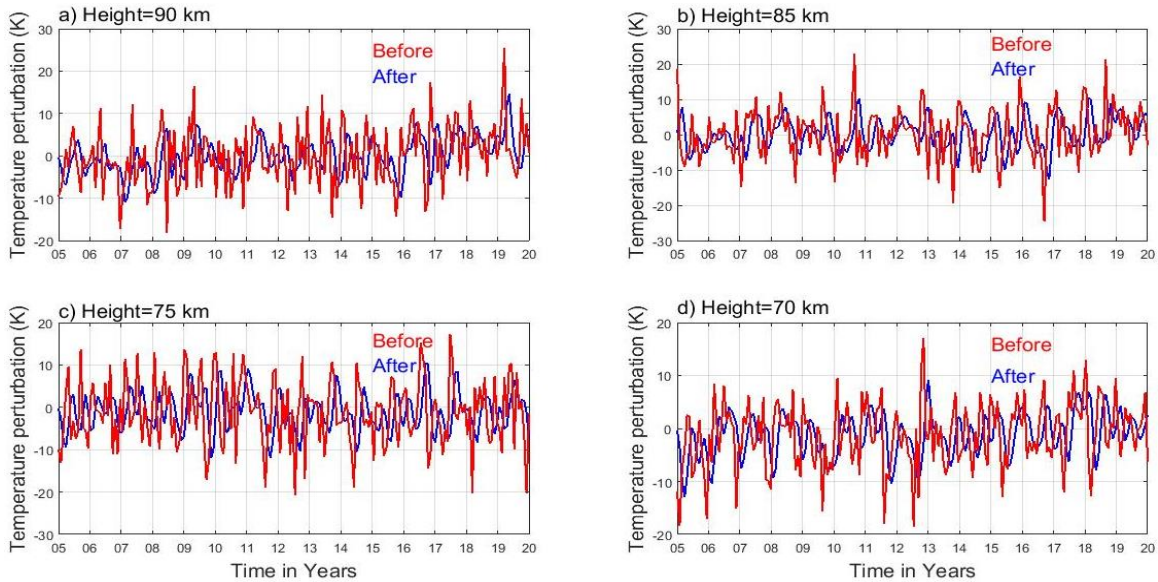


319
 320 **Figure 9.** Same as Figure 7, but for the lower mesosphere atmospheric region.

321 **3.4 Effects of Gravity Waves on Mesosphere Inversions and Associated Instability**

322 Gravity waves form when air parcels oscillate due to the restoring force of gravity after being
 323 transported vertically. Several factors contribute to these waves, including airflow over
 324 mountains, convection, and wind shear. Propagating vertically, the waves break and dissipate,
 325 releasing energy and momentum into the surrounding atmosphere. This process, frequently
 326 responsible for the formation of inversion layers, is further investigated by identifying gravity
 327 wave potential energy (E_p) and its impact on inversion layers at selected MLT regions. This
 328 approach assumes that gravity wave activity is represented by potential energy, as described by
 329 numerous authors (Tsuda et al., 2000; Wang and Geller, 2003; Liu et al., 2014; Thurairajah et al.,
 330 2014). The gravity wave contribution is quantified by calculating the potential energy and
 331 evaluating instability through the Brunt-Väisälä frequency (N^2), derived from perturbed
 332 temperature (T_p') data spanning 2005–2020. The analysis focused on altitudes of 90, 85, 75, and

333 70 km by applying a high-pass filter with a one-hour interval to the T_p ' data (see Figure 10 a-d).
 334 In the upper mesosphere (90 and 85 km), the filter reduces the amplitude of wave oscillations
 335 from approximately ± 20 K to ± 10 K, as shown by the blue curve in Figure 10a and b, compared
 336 to the red curve. Similarly, in the lower mesosphere (75 and 70 km) at (Figure 10 c & d), the
 337 amplitude decreases from $\sim(-20$ to 20 K) to $\sim(-8$ to 8 K) by filtering out higher amplitudes. By
 338 removing the impact of long-period wave oscillations, such as tidal and planetary wave
 339 contributions, the filter effectively isolates the gravity waves (Gw) on the MLT inversions.

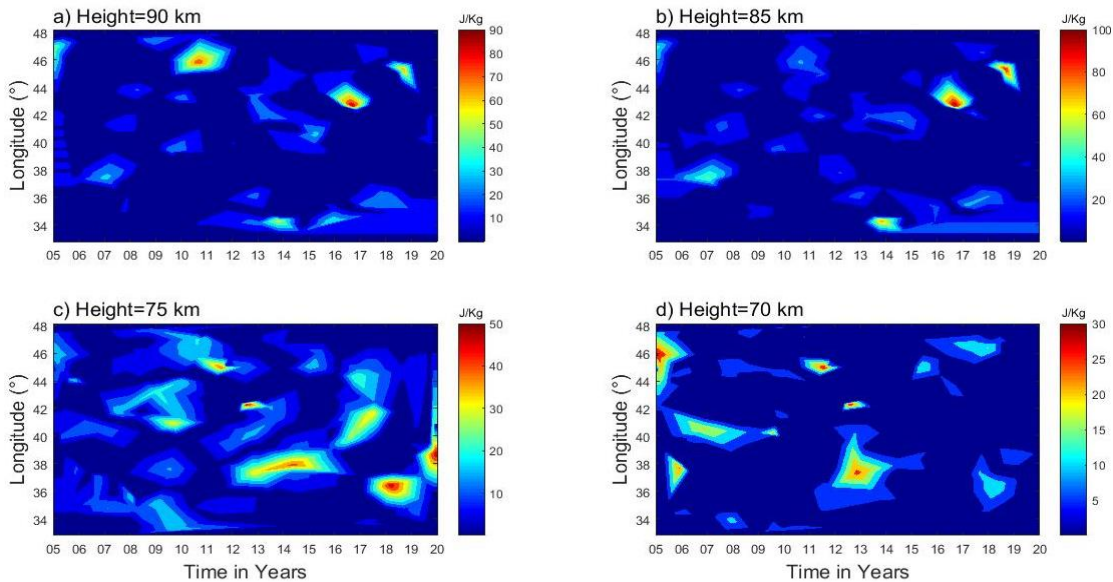


340 **Figure 10.** Perturbed temperature profiles before (red color) and after (blue color) applying the
 341 high-pass filter for the upper (90 and 85 km) and lower (75 and 70 km) regions.
 342

343 In the MLT atmospheric region, gravity wave breaking typically dissipates their potential and
 344 kinetic energy, leading to increased turbulence and mixing. This energy transfer can alter thermal
 345 patterns and impact the overall dynamics of the upper atmosphere. As illustrated, gravity wave
 346 propagation and dissipation are major forces in the MLT region (Lindzen, 1981; Holton, 1983),
 347 influencing middle and upper atmospheric inversions. This has a substantial impact on the
 348 MLT's thermal structure, particularly the increase in temperature variability with elevation,
 349 known as inversion. Holton et al. (2003) and Holton and Hakim (2013) has demonstrated an
 350 interaction between the potential energy of gravity waves and inversions. Interestingly, in this
 351 investigation, the dissipation of gravity waves can lead to the mesospheric inversion layers
 352 (MILs). The study we conducted has clearly shown that the occurrence of an inversion is
 353 maximum at the upper MLT region relative to the lower MLT region from Figure 4. In a
 354 comparable manner, Figure 11 depicts the highest potential energy of gravity waves in the upper

355 MLT regions, demonstrating the interactions between inversion and gravity wave potential
356 energy.

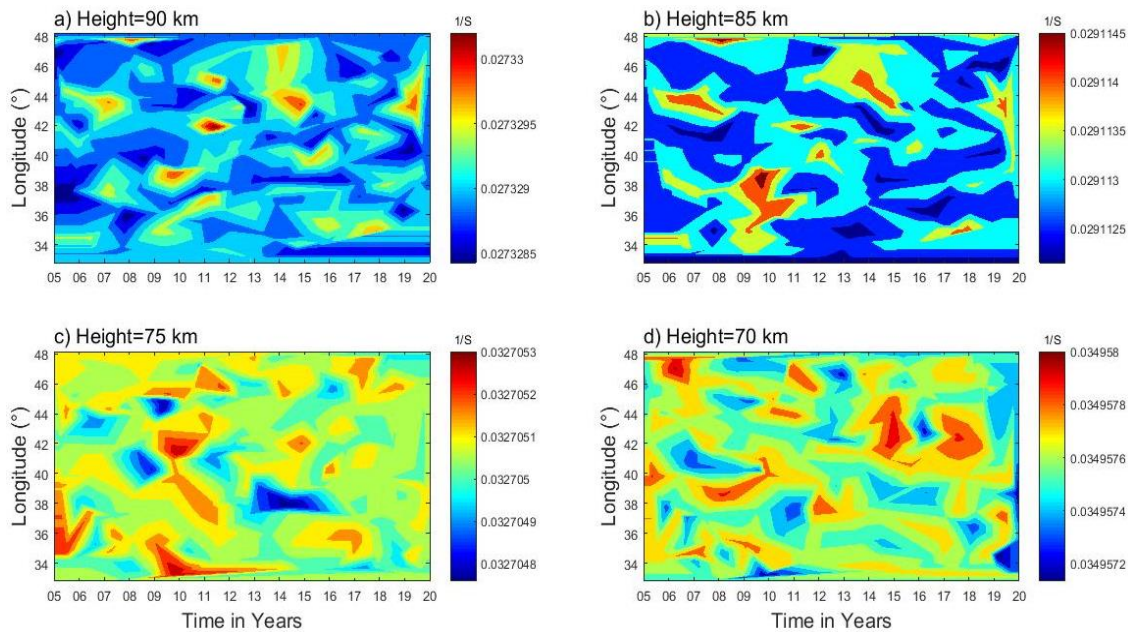
357 Figure 11 (a-d) demonstrates that the spatiotemporal variability of gravity wave potential energy,
358 showing over the upper MLT at (90 and 85 km) and the lower MLT at (75 and 70 km). Figure
359 11(a) of upper MLT inversions at 90 km shows maximum gravity wave potential energies,
360 ranging from ~70 to 90 J/kg, over the longitudinal regions of 45-47° E, as well as at 43° E, and
361 44° E during 2011, 2017, and 2019. In contrast, potential energies around ~10 to 60 J/kg are
362 present across the entire longitudinal region from 33-48° E. Figure 11(b) shows maximum
363 potential energies of ~70 to 100 J/kg over the longitudinal regions of 34°, 44°, and 46° E during
364 2014, 2016, and 2018 at 85 km. Minimum potential energies between 20 and 70 J/kg appear over
365 the longitude regions from 33-48° E. Figures 11(c) and 11(d) depict the gravity wave potential
366 energy in the lower MLT regions at 75 and 70 km, respectively. At 75 km, Figure 11(c) shows a
367 relative maximum potential energy of 40-50 J/kg over the longitudinal regions of 46°, 42°, 40°,
368 37°, 36°, and 38° E during 2011, 2012, 2017, 2013–2015, 2018, and 2020. Similarly, Figure
369 11(d) illustrates gravity wave potential energy ranging from 2-30 J/kg at 70 km across the
370 longitudinal region of 33-48° E. Maximum potential energy of 25-30 J/kg is observed in certain
371 longitudinal regions over time.



372
373 **Figure 11. Gravity wave potential energy for the upper (90 and 85 km) and lower (75 and 70**
374 **km) MLT regions.**

375 Gravity waves generated in different sizes, with smaller waves being the main drivers of
376 instability and turbulence in the MLT (mesosphere and lower thermosphere) region (Liu and

377 Meriwether, 2004; Szewczyk et al., 2013). Hauchecorne et al. (1987) proposed a model where a
 378 series of breaking gravity waves leads to the formation of MILs through the gradual
 379 accumulation of heat, which contributes to instability. **Conducting** mesospheric inversion layer
 380 (MIL) phenomena is crucial for understanding MLT atmospheric dynamics, especially when it
 381 comes to stability and energy transfer. To investigate the role of gravity waves in MLT
 382 instability, the Brunt-Väisälä frequency was used. Contour plots in Figure 12 (a-d) show the
 383 spatiotemporal variability of the Brunt-Väisälä frequency, with Figures 12(a and b) representing
 384 the upper mesosphere (90 and 85 km) and Figures 12(c and d) representing the lower
 385 mesosphere (75 and 70 km). The Brunt-Väisälä frequency (N^2) shows that the upper MLT region
 386 is more unstable (~ 0.027 at 90 km and ~ 0.029 at 85 km) **relative to that of the lower MLT region**
 387 (~ 0.033 at 75 km and ~ 0.035 at 70 km).



388
 389 Figure 12. Brunt-Vaisala frequency (N^2) for the upper (90 and 85 km) and lower (75 and 70 km)
 390 MLT regions.

391 4 Summary

392 In this article, 16 years of SABER MLT temperature profiles are utilized to investigate the MIL
 393 phenomenon and its causative mechanism through gravity wave potential energy (P_E) and
 394 instability criteria of Brunt-Väisälä frequency (N^2) over low latitude bands. The following
 395 conclusions are drawn from the observations in this article:

- 396 ✓ The upper mesosphere inversion frequency occurs more often than the lower mesosphere
 397 inversion.

- 398 ✓ Analysis of the MIL characteristic features reveals the most probable values for the upper
399 inversion: amplitude of 38 k, thickness of 5.5 km, and base height of 78 km. The lower
400 inversion has an amplitude of 25 K, a thickness of 3.8 km, and a base height of 73 km.
- 401 ✓ The upper mesosphere region has higher gravity wave potential energy compared to the
402 lower mesosphere region.
- 403 ✓ The high potential energy in the upper mesosphere region is likely due to the deposition of
404 energy and momentum by gravity wave breaking. This could influence the dynamics of the
405 inversion phenomenon.
- 406 ✓ The Brunt-Väisälä frequency (N^2) indicates that the upper mesosphere region is less stable
407 than the lower mesosphere region. This lower stability contributes to the high potential
408 energy in the upper mesosphere, which leads to larger inversion phenomena.
- 409 ✓ Atmospheric processes vary significantly from region to region, with altitude, and over time.

410 **Data availability.** The SABER data are freely available via the link at [http://saber.gats-inc.com/](http://saber.gats-inc.com/index.php)
411 [index.php](http://saber.gats-inc.com/index.php).

412 **Author contribution.** Chalachew Lingerew: data curation, investigation, software,
413 visualization, writing the original draft, and writing review. U. Jaya Prakash Raju; supervision,
414 and editing.

415 **Competing interest.** The authors declare that they have no conflict of interest relevant to this
416 study.

417 **Acknowledgments.** The Authors would like to express their gratitude to the National Aeronautics
418 and Space Administration (NASA) for providing the SABER data downloaded from the website:
419 <http://saber.gats-inc.com/index.php>.

420 **References**

- 421 Begue, N., Mbatha, N., Bencherif, H., Loua, R. T., Siva Kumar, V., & Leblanc, T.: Statistical
422 analysis of the mesospheric inversion layers over two symmetrical tropical sites:
423 Reunion (20.8° S, 55.5° E) and Mauna Loa (19.5° N, 155.6° W). *In Annales Geophysicae*,
424 35, 1177-1194, 2017.
- 425 Bizuneh, C.L., Prakash, R., and Nigussie, M.: Long-term temperature and ozone response to
426 natural drivers in the mesospheric region using 16 years (2005–2020) of TIMED/SABER
427 observation data at 5-15°N. *Advances in Space Research*, 70, 2095–2111,
428 <https://doi.org/10.1016/j.asr.2022.06.051>, 2022.

429 Collins, R. L., Lehmacher, G. A., Larsen, M. F., and Mizutani, K.: Estimates of vertical eddy
430 diffusivity in the upper mesosphere in the presence of a mesospheric inversion layer, *Ann.*
431 *Geophys.*, 29(11), 2019–2029, <http://doi:10.5194/angeo-29-2019-2011>, 2011.

432 Cutler, L. J., Collins, R. L., Mizutani, K., and Itabe, T.: Rayleigh lidar observations of
433 mesospheric inversion layers at Poker Flat, Alaska (65° N, 14° W), *Geophys. Res. Lett.*, 28,
434 1467–1470, <https://doi.org/10.1029/2000GL012535>, 2001.

435 Dou, X., Li, T., Xu, J., Liu, H. L., Xue, X., Wang, S., Leblanc, T., McDermid, I. S.,
436 Hauchecorne, A., Keckhut, P., Bencherif, H., Heinselman, C., Steinbrecht, W., Mlynczak, M.
437 G., and Russell III, J. M.: Seasonal oscillations of middle atmosphere temperature observed by
438 Rayleigh lidars and their comparisons with TIMED/SABER observations, *J. Geophys. Res.*,
439 114, D20103, <https://doi.org/10.1029/2008JD011654>, 2009.

440 Duck, T. J., Sipler, D. P., and Salah, J. E.: Rayleigh lidar observations of a mesospheric
441 inversion layer during night and day, *Geophys. Res. Lett.*, 28, 3597–3600, 2001.

442 Duck, T. J. and Greene, M. D.: High Arctic observations of mesospheric inversion layers,
443 *Geophys. Res. Lett.*, 31, L02105, <https://doi.org/10.1029/2003GL018481>, 2004.

444 Eckermann, S.D., Hirota, I., and Hocking, W. K.: Gravity wave and equatorial wave morphology
445 of the stratosphere derived from long-term rocket soundings. *Q. J. R. Meteorol. Soc.*, 121, 149
446 186, <http://doi.org/10.1002/qj.49712152108>, 1994.

447 Emanuel, K.A.: *Atmospheric Convection*, Oxford University Press, New York, 580pp, 1994.

448 Fechine, J., Wrasse, C. M., Takahashi, H., Mlynczak, M. G., and Russell, J. M.: Lower-
449 mesospheric inversion layers over Brazilian equatorial region using TIMED/SABER
450 temperature profiles, *Adv. Space Res.*, 41, 1447–1453, [https://doi.org/10.1016/j.asr.2007.](https://doi.org/10.1016/j.asr.2007.04.070)
451 [04.070](https://doi.org/10.1016/j.asr.2007.04.070), 2008.

452 Fritts, D. C., Wang, L., Laughman, B., Lund, T. S., & Collins, R. L.: Gravity wave dynamics in a
453 mesospheric inversion layer: 2. Instabilities, turbulence, fluxes, and mixing. *Journal of*
454 *Geophysical Research: Atmospheres*, 123, 649–670, <https://doi.org/10.1002/2017JD027442>,
455 2018.

456 France, J. A., Harvey, V. L., Randall, C. E., Collins, R. L., Smith, A. K., Peck, E. D., and Fang,
457 X.: A climatology of planetary wave-driven mesospheric inversion layers in the extratropical
458 winter, *J. Geophys. Res.-Atmos.*, 120, 399–413, <https://doi.org/10.1002/2014JD022244>, 2015.

459 Fritts, D. C., and Alexander, M. J.: Gravity wave dynamics and effects in the middle atmosphere,
460 *Rev. Geophys.*, 41, 1003, <https://doi.org/10.1029/2001RG000106>, 2003.

461 Fritts, D. C., Laughman, B., Wang, L., Lund, T. S., & Collins, R. L.: Gravity wave dynamics in a
462 mesospheric inversion layer: 1. Reflection, trapping, and instability dynamics. *Journal of*
463 *Geophysical Research: Atmospheres*, 123, 626-648, <https://doi.org/10.1002/2017JD027440>,
464 2018.

465 Gan, Q., Zhang, S. D., and Yi, F.: TIMED/SABER observations of lower mesospheric inversion
466 layers at low and middle latitudes, *J. Geophys. Res.*, 117, D07109, [https://doi.org/10.1029/2012JD](https://doi.org/10.1029/2012JD017455)
467 [017455](https://doi.org/10.1029/2012JD017455), 2012.

468 Garcia-Comas, M., Lopez-Puertas, M., Marshall, B. T., Winter Steiner, P. P., Funke, B.,
469 Bermejo-Pantaleon, D., Mertens, C. J., Remsberg, E. E., Gordley, L. L., Mlynczak, M. G., and
470 Russell III, J. M.: Errors in Sounding of the Atmosphere using Broadband Emission
471 Radiometry (SABER) kinetic temperature caused by non-local-thermodynamic-equilibrium
472 model parameters, *J. Geophys. Res.*, 113, D24106, doi: 10.1029/2008JD010105, 2008.

473 Hirota, I.: Climatology of gravity waves in the middle atmosphere. *J. Atmos. Terr. Phys.*, 46,
474 767–773, <http://doi.org/10.2151/jmsj1965.63.6-1055>, 1984.

475 Hamilton, K.: Climatological Statistics of Stratospheric Inertia-Gravity Waves Deduced from
476 Historical Rocket-sonde Wind and Temperature Data. *J. Geophys. Res.*, 96, 20831–20839,
477 <http://doi.org/10.1029/91JD02188>, 1991.

478 Hauchecorne, A., Chanin, M. L., & Wilson, R.: Mesospheric temperature inversion and
479 gravity wave breaking. *Geophysical Research Letters*, 14(9), 933-936, [https://doi.org/10.1029/](https://doi.org/10.1029/GL014i009p00933)
480 [GL014i009p00933](https://doi.org/10.1029/GL014i009p00933), 1987.

481 Holton, J. R., Curry, J. A., and Pyle, J. A.: *Encyclopedia of atmospheric sciences*, volume 1.
482 Academic Press, 2003.

483 Holton, J. R.: The influence of gravity wave breaking on the general circulation of the middle
484 atmosphere, *J. Atmos. Sci.*, 40, 2497–2507, 1983.

485 Holton, J. R. and Hakim, G. J.: *An introduction to dynamic meteorology*. Academic Press, 2013.

486 Irving, B. K., Collins, R. L., Lieberman, R. S., Thurairajah, B., and Mizutani, K.: Mesospheric
487 Inversion Layers at Chatanika, Alaska (65°N, 147°W): Rayleigh lidar observations and
488 analysis, *J. Geophys. Res. Atmos.*, 119, 11,235–249, <http://doi.org/10.1002/2014JD021838>, 2014.

489 John, S.R., Kumar, K. K.: TIMED/SABER observations of global gravity wave climatology and
490 their interannual variability from stratosphere to mesosphere lower thermosphere. *Clim. Dyn.*,
491 39, 1489–1505, <http://doi.org/10.1007/s00382-012-1329-9>, 2012.

492 Leblanc, T., McDerimid, I. S., Hauchecorne, A., and Keck hut, P.: Evaluation of optimization of
 493 lidar temperature analysis algorithms using simulated data, *J. Geophys. Res.*, 103, 6177–6187,
 494 1998.

495 Leblanc, T., and Hauchecorne, A.: Recent observations of mesospheric temperature inversions, *J.*
 496 *Geophys. Res.*, 102, 19471–19482, <https://doi.org/10.1029/97JD01445>, 1997.

497 Lindzen, R. S.: Turbulence and stress due to gravity waves and tidal breakdown, *J. Geophys.*
 498 *Res.*, 86, 9707–9714, <https://doi:10.1029/JC086iC10p09707>, 1981.

499 Lingerew, C., Jaya Prakash Raju, U., & Guimarães Santos, C. A.: NN-MLT model prediction for
 500 low-latitude region based on artificial neural network and long-term SABER observations.
 501 *Earth and Space Science*, 10, e2023EA002930, <https://doi.org/10.1029/2023 EA002930>, 2023.

502 Liu, S-D., and S-S. Liu: *Atmosphere Dynamics*, Peking University Press, Beijing, 2011.

503 Liu, H. L., Hagan, M. E., & Roble, R. G.: Local mean state changes due to gravity wave
 504 breaking modulated by the diurnal tide. *Journal of Geophysical Research*, 105(D10),
 505 12381-12396, (2000).

506 Liu, H. L., & Hagan, M. E.: Local heating/cooling of Atmospheres. 96(D8), 15297-15309,
 507 (1998).

508 Mlynczak, M. G., Marshall, B. T., Martin-Torres, F. J., Russell III, J. M., Thompson, R. E.,
 509 Remsberg, E. E., and Gordley, L. L.: Sounding of the Atmosphere using Broadband Emission
 510 Radiometry observations of daytime mesospheric O₂ (1Δ) 1.27 μm emission and derivation of
 511 ozone, atomic oxygen, and solar and chemical energy deposition rates, 2007.

512 Meriwether, J. W., and Gerrard, A. J.: Mesosphere inversion layers and stratosphere temperature
 513 enhancements, *Rev. Geophys.*, 42, RG3003, <http://doi:10.1029/2003RG000133>, 2004.

514 Meriwether, J. W., and Gardner, C. S.: A review of the mesosphere inversion layer phenomenon,
 515 *J. Geophys. Res.*, 105, 12 405–12 416, 2000.

516 Nath, O., & Sridharan, S.: Long-term variabilities and tendencies in zonal mean TIMED–
 517 SABER ozone and temperature in the middle atmosphere at 10–15°N. *Journal of Atmospheric*
 518 *and Solar-Terrestrial Physics*, 120, 1–8, <https://doi:10.1016/j.jastp.2014.08.010>, 2014.

519 Ramesh, K., Sridharan, S.: Large mesospheric inversion layer due to breaking of small scale
 520 gravity waves: Evidence from Rayleigh lidar observations over Gadanki (13.51⁰ N, 79.21⁰ E).
 521 *J. Atmos. Sol. Terr. Phys.* 89, 90–97, <http://doi.org/10.1016/j.jastp.2012.08.011>, 2012.

522 Ramesh, K., Sridharan, S. and Vijaya Bhaskara, S.: Causative mechanisms for the occurrence of
 523 a triple-layered mesospheric inversion event over low latitudes, *J. Geophys. Res. Space*
 524 *Physics*, 119, 3930–3943, <http://doi:10.1002/2013JA019750>, 2014.

525 Ramesh, K., Sridharan, S., Raghunath, K., and Rao, S. V. B.: A chemical perspective of day and
526 night tropical (10°N–15°N) mesospheric inversion layers, *J. Geophys. Res. Space Physics*,
527 122, <http://doi:10.1002/2016JA023721>, 2017.

528 Ramesh, K., Sridharan, S., Vijaya Bhaskara Rao, S., Raghunath, K., Bhavani Kumar, K.:
529 Rayleigh lidar observations of mesospheric inversion layers over Gadanki (13.5°N, 79.2° E)
530 and their relation with gravity wave activities. *Indian Journal of Radio and Space Science*, 43,
531 83-90, 2013.

532 Remsberg, E., Lingenfelter, V., Harvey, V., Grose, W., Russell III, J., Mlynczak, M., Gordley,
533 L., and Marshall, B. T.: The verification of the quality of SABER temperature, geopotential
534 height, and wind fields by comparison with Met Office assimilated analyses, *J. Geophys. Res.*,
535 108(D19), 4628, <https://doi:10.1029/2003JD003720>, 2003.

536 Rezac, L., Kutepov, A., Russell, J.M., Feofilov, A.G., Yue, J., and Goldberg, R.A.: Simultaneous
537 retrieval of T (p) and CO₂ VMR from two-channel non-LTE limb radiances and application to
538 daytime SABER/ TIMED measurements. *J. Atmos. Sol. Terr. Phys* 130–131, 23–42.
539 <https://doi.org/10.1016/j.jastp.2015.05.004>, 2015.

540 Russell, J.M., Mlynczak, M.G., Gordley, L.L., Tansock, J., Esplin, R.: An overview of the
541 SABER experiment and preliminary calibration results. In *Proceedings of the SPIE, 44th*
542 *Annual Meeting, Denver, CO, USA, 3756, 277–288*, 1999.

543 Schmidlin, F. J.: Temperature inversions near 75 km. *Geophysical Research Letters*, 3(3),
544 173-176, (1976).

545 Sica, R. J., Argall, P. S., Shepherd, T. G., and Koshyk, J. N.: Model-measurement comparison of
546 mesospheric temperature inversions, and a simple theory for their occurrence, *Geophys. Res.*
547 *Lett.*, 34, L23806, <https://doi:10.1029/2007GL030627>, 2007.

548 Sivakandan, M., Kapasi, D., and Taori, A.: The occurrence altitudes of middle atmospheric
549 temperature inversions and mesopause over low-latitude Indian sector, *Ann. Geophys.*, 32,
550 967–974, <https://doi.org/10.5194/angeo-32-967-2014>, 2014.

551 Siva Kumar, V., Bhavani Kumar, Y., Raghunath, K., Rao, P. B., Krishnaiah, M., Mizutani, K.,
552 Aoki, T., Yasui, M., and Itabe, T.: Lidar measurements of mesospheric temperature inversion
553 at a low latitude, *Ann. Geophys.*, 19, 1039–1044, <https://doi.org/10.5194/angeo-19-1039-2001>,
554 2001.

555 Sridharan, S., Sathishkumar, S., and Gurubaran, S.: Influence of gravity waves and tides on
556 mesospheric temperature inversion layers: simultaneous Rayleigh lidar and MF radar
557 observations, *Ann. Geophys.*, 26, 3731–3739, 2008.

558 Singh, R. P., & Pallamraju, D.: Mesospheric temperature inversions observed in OH and O2
559 rotational temperatures from Mount Abu (24.6°N, 72.8°E), India. *Journal of Geophysical*
560 *Research: Space Physics*, 123, 8823–8834, <https://doi.org/10.1029/2018JA025703>, 2018.

561 Smith, A.: Global Dynamics of the MLT, *Surv. Geophys*, 33, 1177–1230,
562 <https://doi.org/10.1007/s10712-012-9196-9>, 2012.

563 Szewczyk, A., Strelnikov, B., Rapp, M., Strelnikova, I., Baumgarten, G., Kaifler, N., Dunker, T.,
564 and Hoppe, U. P.: Simultaneous observations of a Mesospheric Inversion Layer and turbulence
565 during the ECOMA-2010 rocket campaign, *Ann. Geophys.*, 31, 775–785, [http://doi:10.5194/](http://doi:10.5194/angeo-31-775-2013)
566 [angeo-31-775-2013](http://doi:10.5194/angeo-31-775-2013), 2013.

567 Vadas, S. L., and Fritts, D. C.: Thermosphere responses to gravity waves: Influences of
568 increasing viscosity and thermal diffusivity, *J. Geophys. Res.*, VOL. 110, D15103, doi:
569 [10.1029/2004JD005574](https://doi.org/10.1029/2004JD005574), 2005.

570 Wang, L., Geller, M.A., Alexander, M.J.: Spatial and Temporal Variations of Gravity Wave
571 Parameters. Part I: Intrinsic Frequency, Wavelength, and Vertical Propagation Direction. *J.*
572 *Atmos. Sci.*, 62, 125–142, <http://doi.org/10.1029/2010JD013860>, 2005.

573 Wang, L., and Alexander, M.J.: Global estimates of gravity wave parameters from GPS radio
574 occultation temperature data. *J. Geophys. Res.* 115, D21122, <http://doi.org/10.1029/2010J>
575 [D013860](http://doi.org/10.1029/2010JD013860), 2010.

576 Walterscheid, R. L., and Hickey, M. P.: Gravity wave ducting in the upper mesosphere and lower
577 thermosphere duct system, *J. Geophys. Res.*, 114, D19109, <http://doi:10.1029/2008JD011269>,
578 2009.

579 Yuan, T., Pautet, P. D., Zhao, Y., Cai, X., Criddle, N. R., Taylor, M. J., and Pendleton, W. R.:
580 Coordinated investigation of mid-latitude upper mesospheric temperature inversion layers and
581 the associated gravity wave forcing in Logan, Utah, *J. Geophys. Res. Atmos.*, 119, 3756–3769,
582 <http://doi:10.1002/2013JD020586>, 2014.